Bi-doped Ceria with Increased Oxygen Vacancy for Enhanced CO$_2$ Photoreduction Performance

LIU Yaxin[1,2], WANG Min[1,2], SHEN Meng[1,2], WANG Qiang[1,2], ZHANG Lingxia[1,2]

(1. State Key Laboratory of High Performance Ceramics and Superfine Microstructure, Shanghai Institute of Ceramics, Chinese Academy of Sciences, Shanghai 200050, China; 2. Center of Materials Science and Optoelectronics Engineering, University of Chinese Academy of Sciences, Beijing 100049, China)

Abstract: Oxygen vacancy plays an important role in promoting CO$_2$ adsorption and reduction on photocatalysts. Bi was heavily doped into ceria, forming a solid solution catalyst Ce$_{1-x}$Bi$_x$O$_{2-\delta}$ meanwhile maintaining the fluorite structure, to increase the oxygen vacancy concentration. The sample Ce$_{0.6}$Bi$_{0.4}$O$_{2-\delta}$ showed the highest photocatalytic activity with a CO yield of ~4.6 times that of the pristine ceria nanorods. Bi was homogeneously dispersed into the fluorite ceria which was confirmed by XRD and EDX elemental mapping. It has been evidenced by the results of Raman and XPS that Bi introduction boosts the concentration of oxygen vacancy in the solid solution that can facilitate the adsorption/activation of carbonate and bicarbonate intermediates on its surface according to *in-situ* FT-IR.

Key words: photocatalysis; CeO$_2$; CO$_2$ reduction; Bi; oxygen vacancy

Solar energy driving CO$_2$ conversion into valuable chemicals is a promising way to tackle the dilemma of climate crisis and energy shortage[1]. Since the discovery that TiO$_2$ can be used to reduce H$_2$O and CO$_2$, a variety of semiconductor photocatalysts have been fabricated to increase the photo-to-chemical efficiency. Based on these materials, a series of improvement strategies have been developed, such as defect engineering[2], surface plasmon sensitization[3], element doping, and heterojunction construction[4]. Most strategies gain improved photocatalytic performance by increasing visible light absorption[5], promoting charge separation/transfer and enhancing CO$_2$ adsorption/activation.

Among the recent reports on metal oxide based photocatalysts, oxygen vacancy (O$_v$) engineering has been found to be a facile and effective way to improve photoactivity on all respects. Formation of O$_v$ in Bi$_2$MoO$_6$ created a defect energy level in the band gap and enhanced the visible-light-driven photocatalytic activity of Bi$_2$MoO$_6$[6]. Our previous work introduced Cu into CeO$_{2-x}$ to generate and stabilize the surface oxygen vacancies (O$_{vs}$) and achieved high CO$_2$ photoreduction activity[7]. Though researchers have made great efforts to

explore the effects of O$_v$ on catalysts' chemical/physical properties and photocatalytic reaction process by experiments and theoretical calculations, there are still some issues to be clarified based on rational material design and advanced characterizations, especially *in-situ* or *operando* investigations.

Typically, ceria-based oxides serve as an active oxygen donor in a wide range of reactions[8]. It is worth noting that both Ce^{3+} and Ce^{4+} can exist stably because of their unique electronic configurations. To balance the charge, active oxygen is released spontaneously and O$_v$ is formed, which can be usually recovered when exposed to an oxidative environment. Due to this unique nature, great efforts have been made to create O$_v$ and clarify the effects of O$_v$ in CeO$_2$. In order to demonstrate the effect and behavior of the as-formed O$_v$ in CeO$_2$, bismuth is selected as a dopant that is expected to maintain the fluorite structure and the stability of O$_v$ because of its lower valence state (+3) and its ion radius (0.117 nm) similar to Ce^{4+} (0.097 nm)[9]. Here we synthesized and explored a Ce$_{1-x}$Bi$_x$O$_{2-\delta}$ solid solution photocatalyst with boosted O$_v$ concentration and enhanced CO$_2$ photoreduction ability under ambient environment. A series of Ce$_{1-x}$Bi$_x$O$_{2-\delta}$

oxide catalysts were investigated and the catalyst with an optimal Bi/(Bi+Ce) ratio of 0.4 exhibited highest CO_2 photoreduction efficiency. The relationship between the O_v concentration and the photocatalytic activity of $Ce_{1-x}Bi_xO_{2-\delta}$ solid solution catalyst was explored by structural, compositional and *in-situ* FT-IR characterizations.

1　Experimental

1.1　Preparation of catalysts

Samples were synthesized by a facile one-step hydrothermal process at controlled conditions. Typically, a certain amount of $Ce(NO_3)_3 \cdot 6H_2O$ and $Bi(NO_3)_3 \cdot 5H_2O$ were dissolved in diluted nitrite acid (HNO₃, 5 mL, 4 mol/L) by sonication before the dropwise addition of 8 mol/L aqueous solution of NaOH (35 mL) while stirring. This mixture was kept stirring for 30 min till the formation of a gelatinous suspension and then transferred into a 50 mL Teflon-lined autoclave within a stainless-steel tank and placed at 100 ℃ for 24 h. The obtained samples were rinsed in deionized water and washed with anhydrous ethanol for several times. Then the powder was oven-dried overnight in vacuum at 60 ℃. The samples were denoted as $Ce_{1-x}Bi_xO_{2-\delta}$, where x represents the molar ratio of Bi/(Ce+Bi). The sample synthesized with $Ce(NO_3)_3 \cdot 5H_2O$ (1.5 g) as the sole precursor under the same conditions was named as CeO_2.

1.2　Characterizations

X-ray diffraction patterns (XRD) of the samples were recorded on Rigaku D/Max 2200PC X-ray diffractometer. The measurement was operated at room temperature under Cu Kα radiation with a scanning rate of 4 (°)/min. A JEM-2100F field emission transmission electron microscope (TEM) (200 kV) was used to obtain the TEM image. Ultraviolet visible (UV-Vis) absorption spectra (800 nm to 200 nm) were recorded by a UV-3101 PC Shimadzu spectroscope (BaSO₄ as the reference standard material). Electron paramagnetic resonance (EPR) spectra were obtained from a Bruker EMXplus (Germany) spectrometer at 90 K. X-ray photoelectron spectra (XPS) were obtained on a Thermo Scientific ESCALAB 250 spectrometer with multichannel detector, Al Kα radiation as excitation source, and C1s at 284.6 eV as a signal-calibrating standard of binding-energy values. Time-resolved fluorescence spectra were tested on an Edinburgh Instruments FLS920 spectrometer under 420 nm excitation of deuterium lamp. DXR Raman microscope was used to obtain Raman spectra under the excitation of 532 nm. *In-situ* Fourier transform infrared (FT-IR) spectra were collected in N_2 and CO_2, respectively, on Nicolet iS10 equipped with MCT detector. The catalyst was swept by N_2 for 1 h and stabilized for 1 h before the FT-IR spectrum was collected and saved as background data. Subsequently, the catalyst was swept by CO_2 for 1 h and stabilized for 1 h. Then the *in-situ* FT-IR spectra were recorded at different time intervals since the beginning of light irradiation.

1.3　Electrochemical measurements

Electrochemical measurements were conducted on a CHI660A electrochemical workstation (Shanghai Chenhua, China) with a standard three-electrode system. Fluorine-doped tin oxide (FTO) glass deposited (15 mm× 25 mm) with photocatalyst as the working electrode, platinum wire and Ag/AgCl as counter electrode and reference electrode, respectively. The electrolyte was 0.2 mol/L Na_2SO_4 aqueous solution. The preparation process of working electrodes by electrophoretic deposition was as follows: sample powder (20 mg) and iodine (10 mg) were mixed and well milled in an agate mortar then well-dispersed in acetone (30 mL). Thus, the plating solution was obtained. A thin film of the sample was uniformly deposited on FTO with a potentiostat bias of 10 V for 10 min and then calcined in an oven at 150 ℃ for 2 h. During the electrochemical measurement, the coated area of all samples was controlled at 1 cm². Mott-Schottky plots were obtained by impedance-potential tests at the frequency of 1000 Hz with a voltage amplitude of 10 mV. Nyquist plots were tested in dark at a bias voltage of –0.4 V *vs* Ag/AgCl electrode. With irradiation from a 300 W Xe arc lamp, the transient photocurrent densities were obtained at 0.3 V *versus* Ag/AgCl electrode.

1.4　Photocatalytic activity evaluation

The light source was a 300 W Xenon arc lamp from Aulight CEL-HX, Beijing, the light intensity of which tested on the position of catalyst was 210 mW/cm². The gas products (CO, CH₄) were analyzed by GC-2014 gas chromatograph (flame ionization detector, FID) equipped with a 0.5 nm molecular column and a TDX-01 packed column. The photocatalysis test was conducted typically as follows: 50 mg of photocatalyst was uniformly dispersed on a 2.5 cm × 2.5 cm glass at the bottom of a 625 mL sealed glass reactor. The temperature of the reactor was kept at 15 ℃ with cooling water circulation. To exclude possible influence of contaminants, the sealed reactor was filled with N_2 and subjected to the irradiation of Xe lamp for 2 h before CO_2 (99.99% of purity) moisturized by a water bubbler was pumped into the reactor and stabilized for 30 min. During the photoreaction, 1 mL of sample gas was continually extracted from the reactor every 1 h and analyzed on GC according to external standard method. Before each activity (or cycle)

test, the photocatalyst was firstly heat-treated at 150 ℃ for 2 h, so as to remove the organic impurities and adsorbed carbon species.

2 Results and discussion

2.1 Improved photocatalytic activity of $Ce_{1-x}Bi_xO_{2-\delta}$ in CO_2 reduction reaction

A series of $Ce_{1-x}Bi_xO_{2-\delta}$ (x=0, 1, 2, 3, 4, 5) samples were synthesized by co-precipitation method and all catalysts were tested for gas-solid phase CO_2 reduction in sealed glass reactor under the conditions of 15 ℃, 1×10^5 Pa. CO was the main product with trace CH_4 detected. Controlled experiments without light irradiation, CO_2, or photocatalysts were conducted, in which no CO was detected, proving that CO was derived from CO_2 photoreduction. As displayed in Fig. 1, with the increase of Bi content, the catalytic performance of the samples improves. $Ce_{0.6}Bi_{0.4}O_{2-\delta}$ shows the highest activity in CO_2 photoreduction with a CO yield of 0.5 $\mu mol \cdot g^{-1} \cdot h^{-1}$ under Xe light irradiation, which is ~4.6 times of that on CeO_2.

2.2 Chemical and structural characterizations

XRD patterns (Fig. S1) show that the $Ce_{1-x}Bi_xO_{2-\delta}$ solid solution samples prepared in this work maintained the fluorite cubic structure of ceria (JCPDS 34–0394). With Bi content ranging from 10% to 50%, all peaks broaden and shift slightly towards small angle, which indicates that adding Bi into ceria increased the lattice parameter. The morphology of the as-prepared ceria and $Ce_{0.6}Bi_{0.4}O_{2-\delta}$ were further characterized by TEM (Fig. 2). Pure ceria shows the morphology of granite nanorods, 100–300 nm in length and 12–20 nm in diameter (Fig. 2(a)) while $Ce_{0.6}Bi_{0.4}O_{2-\delta}$ is in the form of nanocubes with particle size of ~35 nm (Fig. 2(b)). The substitution of Ce^{4+} atom with Bi^{3+} distorted the crystal structure and changed the crystal growth behavior,

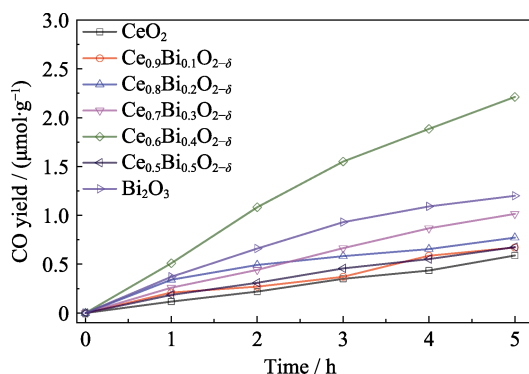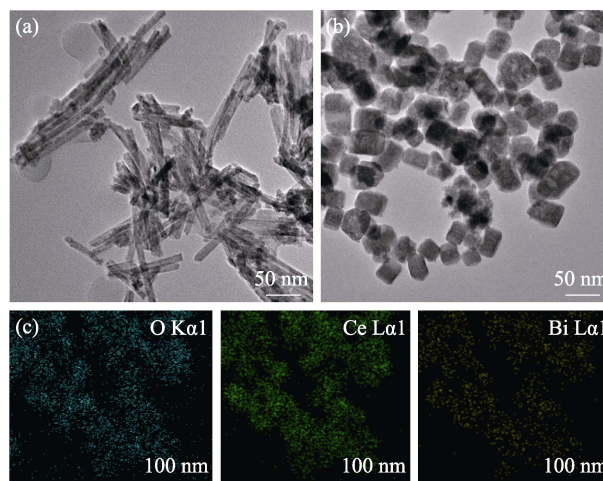Fig. 2 TEM images of (a) CeO_2 and (b) $Ce_{0.6}Bi_{0.4}O_{2-\delta}$, (c) EDX elemental mapping images of $Ce_{0.6}Bi_{0.4}O_{2-\delta}$

leading to surface reconstruction and defects, which can be confirmed by the bright spots observed in $Ce_{0.6}Bi_{0.4}O_{2-\delta}$ nanocubes[10]. Fig. 2(c) shows that O, Ce, and Bi distribute homogeneously in the $Ce_{0.6}Bi_{0.4}O_{2-\delta}$ sample. No segregation has been observed and a solid solution catalyst can be identified.

To further probe the chemical and compositional differences Bi doping induced, XPS spectra were collected to analyze the chemical states of Ce, Bi and O on the surface of CeO_2 and $Ce_{0.6}Bi_{0.4}O_{2-\delta}$ samples. There are multiple peaks in the Ce3d XPS spectra (Fig. 3(a)). Both CeO_2 and $Ce_{0.6}Bi_{0.4}O_{2-\delta}$ show eight major characteristic peaks located at 917.9, 916.6, 907.2, 900.7, 898.5, 889.7, 886.5 and 882.3 eV (spin-orbit splitting peaks), which are uniquely attributed to Ce^{4+}, thus the main valence state of Ce can be identified as +4. The presence of Ce^{3+} can be also distinguished in both CeO_2 and $Ce_{0.6}Bi_{0.4}O_{2-\delta}$ by the peaks at 902.5 and 884.2 eV(denoted as v_1 and v_2). Through the comparison of these two characteristic peaks (v_1 and v_2) corresponding to Ce^{3+}, especially against the concurrent decrease of the two adjacent peaks(u_1 and u_2) of Ce^{4+}, we are convinced of that, with the introduction of Bi into ceria lattice, Ce^{3+} increases in $Ce_{0.6}Bi_{0.4}O_{2-\delta}$[3]. While in Fig. 3(b), the representative core level Bi4f spectrum shows that Bi^{3+} exists exclusively in nanocrystalline solid solution $Ce_{0.6}Bi_{0.4}O_{2-\delta}$[10]. Two highly symmetric peaks are located at 158.8 eV for Bi $4f_{7/2}$ and 164.1 eV for Bi$4f_{5/2}$, which agree well with those observed in standard bismuth oxides[11]. This result combined with those of XRD and TEM demonstrates that Ce atoms have been successfully substituted by Bi atoms in CeO_2 lattice and a solid solution catalyst has been formed.

The O1s spectra of the samples (Fig. 3(c)) can be deconvoluted into three peaks. For CeO_2, the two peaks at 529.2 and 529.7 eV are assigned to lattice oxygen

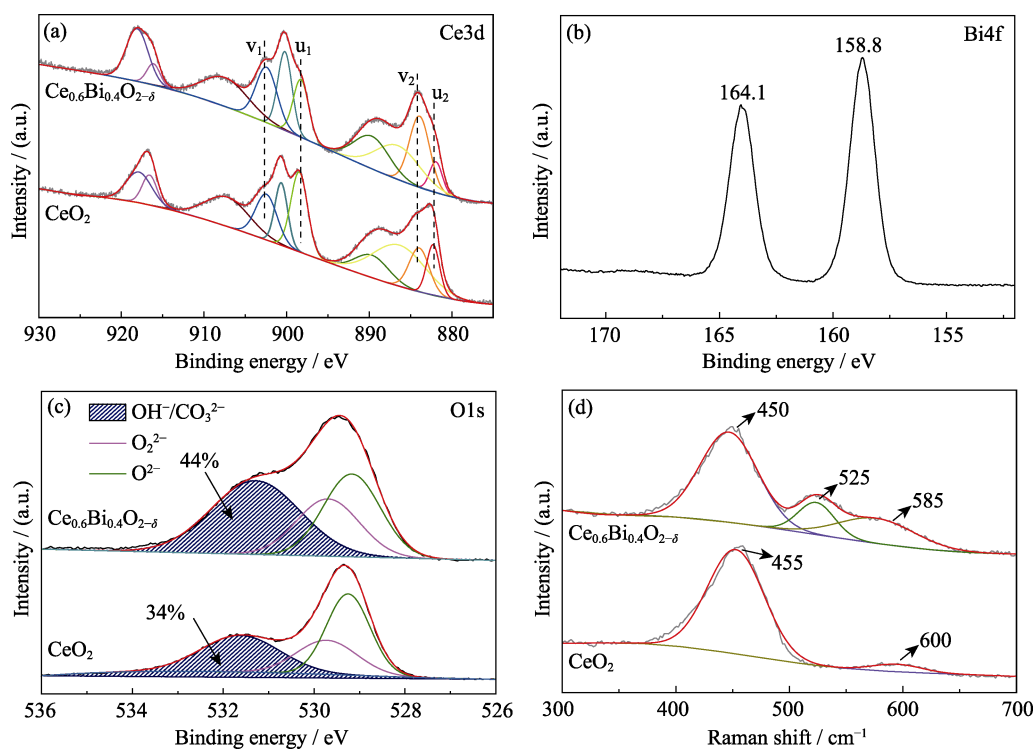Fig. 1 Time-dependent CO evolution over CeO_2, $Ce_{1-x}Bi_xO_{2-\delta}$ and Bi_2O_3

Fig. 3   High resolution XPS spectra of (a) Ce3d, (b) Bi4f, (c) O1s on the surface of Ce$_{0.6}$Bi$_{0.4}$O$_{2-\delta}$ and (d) Raman spectra of CeO$_2$ and Ce$_{0.6}$Bi$_{0.4}$O$_{2-\delta}$

species (O$_{latt}$), O^{2-} and O$_2^{2-}$, respectively[2]. The peak at 531.6 eV is ascribed to adsorbed oxygen species (O$_{ad}$)[12-13]. It is noted that there is slight band shift of O$_{ad}$ to lower binding energy in the O1s spectra of Ce$_{0.6}$Bi$_{0.4}$O$_{2-\delta}$ than in CeO$_2$ and the signal increases, suggesting the adsorbed H$_2$O and CO$_2$ are more easily to get electrons from the surface of Ce$_{0.6}$Bi$_{0.4}$O$_{2-\delta}$, that is, are more readily to be activated on the reactive sites after the introduction of O$_{vs}$ together with Bi. The O$_{ad}$ content calculated from peak area, which is proportional to that of O$_v$, is 44%, much higher in Ce$_{0.6}$Bi$_{0.4}$O$_{2-\delta}$ than 34% in CeO$_2$. This means our intention of modulating O$_v$ content by Bi-doping is feasible.

In the Raman spectra (Fig. 3(d)), CeO$_2$ and Ce$_{0.6}$Bi$_{0.4}$O$_{2-\delta}$ exhibit distinct vibrational bands at 350−650 cm^{-1}. For pristine CeO$_2$, the band at 455 cm^{-1} is ascribed to the F$_{2g}$ vibration mode of CeO$_2$ fluorite while the weak signal at about 600 cm^{-1} is related to the intrinsic O$_{vs}$ due to the existence of Ce^{3+}[14]. Compared with pure CeO$_2$, major differences appear in the Raman vibration modes of Ce$_{0.6}$Bi$_{0.4}$O$_{2-\delta}$ in that the F$_{2g}$ band shifts to low frequency (about 450 cm^{-1}) and slightly broadens. This phenomenon is explained as that the symmetrical stretching vibration of Ce[O]$_8$ unit is distorted by Bi doping. The second vibration mode of Ce$_{0.6}$Bi$_{0.4}$O$_{2-\delta}$ located at 525 cm^{-1} can be indexed to the presence of Bi^{3+}. More importantly, the signal around 585 cm^{-1}, which is related to extrinsic O$_{vs}$ that serve as charge-compensating defects, is significantly

strengthened[15-17]. Here, it can be concluded that Bi doping in CeO$_2$ has boosted the presence of O$_{vs}$. For Ce$_{0.6}$Bi$_{0.4}$O$_{2-\delta}$, the half-width at half-maximum (HWHM) at 450 cm^{-1} is ~29.8 cm^{-1}, based on which the intrinsic O$_{vs}$ concentration is calculated to be ~2.34×10^{21} cm^{-3}. It is higher than that of the pristine CeO$_2$ (2.10×10^{21} cm^{-3}). This can be also verified by the enhancement of EPR signal at *g*-value of 2.003 corresponding to O$_{vs}$ of Ce$_{1-x}$Bi$_x$O$_{2-\delta}$ compared with that of CeO$_2$ in Fig. S2. In following discussions, corresponding implications on the catalytic activity of the solid solution catalyst will be illustrated from aspects including visible light absorption, electrochemical performance and CO$_2$ adsorption/activation.

UV-Vis diffuse absorbance spectra of all the samples were recorded as displayed in Fig. S3. Compared with pure ceria, all Ce$_{1-x}$Bi$_x$O$_{2-\delta}$ solid solution samples show enhanced and red-shifted absorption. Among them, samples Ce$_{0.6}$Bi$_{0.4}$O$_{2-\delta}$ and Ce$_{0.5}$Bi$_{0.5}$O$_{2-\delta}$ show the strongest UV-visible light absorption that extends from 380 nm to around 500 nm. The result and the yellow color of the solid solution catalyst (pure ceria is white) indicate that the introduction of Bi can successfully extend the light response to UV-visible region, which can be attributed to the defect energy level generated from the increased O$_v$ concentration. Based on the UV-Vis diffuse absorbance spectra and Kubelka-Munk equation[18] for indirect gap semiconductors, the bandgaps of pure ceria and Ce$_{0.6}$Bi$_{0.4}$O$_{2-\delta}$ were estimated to be 3.1 and 2.6 eV, res-

pectively. This bandgap narrowing caused by Bi incorporation and O_v can initiate the effective visible light induced photocatalytic CO_2 reduction reaction.

To better understand the influence of Bi doping on the energy band structure of the solid solution catalyst, the Mott-Schottky plots of CeO_2 and $Ce_{0.6}Bi_{0.4}O_{2-\delta}$ electrodes were analyzed, both of which are S-type curves of n-type semiconductors (Fig. S4(a)). The flat band potentials (V_{fb}) were estimated from the linear part of the plots as –0.59 and –0.48 V vs Ag/AgCl electrode for CeO_2 and $Ce_{0.6}Bi_{0.4}O_{2-\delta}$, respectively. According to literature, the conduction band potential (E_{cb}) of one n-type semiconductor is 0–0.2 V more negative than its V_{fb}, depending on carrier concentration and effective mass of electron. Here, the potential difference is set as 0.1 V. Based on this result, the band structure can be reasonably estimated in which a downshift of E_{cb} (from –0.7 V of CeO_2 to –0.6 V of $Ce_{0.6}Bi_{0.4}O_{2-\delta}$) and an upshift of E_{vb} (from 2.4 V of CeO_2 to 2 V of $Ce_{0.6}Bi_{0.4}O_{2-\delta}$) are clearly illustrated. This band narrowing happens when the Bi6p and Bi6s orbits participate in the construction of CB and VB, respectively[12].

EIS Nyquist plots of the as-obtained samples in dark demonstrate that $Ce_{0.6}Bi_{0.4}O_{2-\delta}$ is much more conductive than CeO_2 (Fig. S4(b)). This is because that ceria is a kind of good ion conductive solid electrolyte and O_v can promote ion transportation[13] and thus endows the $Ce_{0.6}Bi_{0.4}O_{2-\delta}$ solid solution catalyst better conductivity which could efficiently promote the separation and interfacial transmission of photoexcited carriers. As a result, the photocurrent response of $Ce_{0.6}Bi_{0.4}O_{2-\delta}$ nearly triples over that of CeO_2 (Fig. S5).

2.3 *In-situ* probe into the catalytic mechanism of CO_2 photoreduction on $Ce_{0.6}Bi_{0.4}O_{2-\delta}$

Based on the electronic structure estimation, a possible CO_2 photoreduction mechanism is proposed in Fig. 5. To further understand the origin of enhanced CO_2 photocatalytic reduction activity of the solid solution catalyst, *in-situ* FT-IR spectroscopy was used to investigate the adsorption, activation, and conversion process of CO_2 on $Ce_{0.6}Bi_{0.4}O_{2-\delta}$ and CeO_2. The *in-situ* FT-IR spectra of CO_2 adsorption on CeO_2 and $Ce_{0.6}Bi_{0.4}O_{2-\delta}$ swept by humid CO_2 and stabilized for 1 h were collected and shown in Fig. 4(a, b), respectively. Similar modes of carbonate signals after humid CO_2 sweeping can be observed on the surface of the catalysts, with those of $Ce_{0.6}Bi_{0.4}O_{2-\delta}$ more intense[14]. Specifically, the band at ~1700 cm^{-1} corresponds to bicarbonate (HCO_3^-)[15]. The bands at about 1510 and 1380 cm^{-1} are assigned to mono-dentate carbonate (m-CO_3^{2-})[16]. The bands at about 1337 and 1422 cm^{-1} correspond to bidentate carbonate (b–CO_3^{2-})[17]. The peaks at about 1255, 1610 and 1650 cm^{-1} are assigned
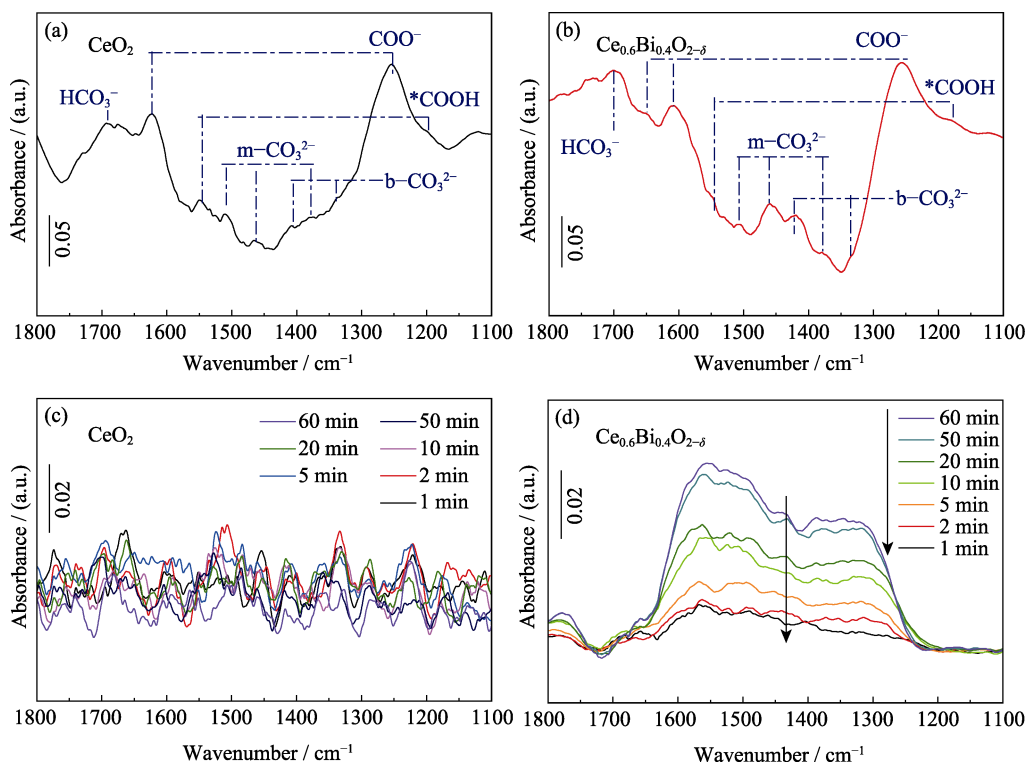

Fig. 4 *In-situ* FT-IR spectra of CO_2 adsorption on the surface of (a) CeO_2 and (b) $Ce_{0.6}Bi_{0.4}O_{2-\delta}$
(the spectra of the samples swept by N_2 for 1 h as the background);
In-situ FT-IR spectra of CO_2 photoreduction on (c) CeO_2 and (d) $Ce_{0.6}Bi_{0.4}O_{2-\delta}$ at different irradiation time
(The spectra collected at 0 min of irradiation in humid CO_2 as background)

to the bending vibration of carboxylate (COO⁻)[18] while the bands at about 1550 and 1200 cm⁻¹ are ascribed to *COOH. The existence of –CO_3^{2-} is due to the formation of carbonic acid and the adsorbed CO_2 on the catalyst surface[2].

After Xe light irradiation, the *in-situ* FT-IR spectra of CeO_2 and $Ce_{0.6}Bi_{0.4}O_{2-\delta}$ were collected and shown in Fig. 4(c, d), respectively. Over irradiation time, the clear increase and decrease of signals that is corresponding to the generation and consumption of the adsorbed intermediates on the surface of $Ce_{0.6}Bi_{0.4}O_{2-\delta}$ emerges while those on CeO_2 remain indiscernible. The aforementioned IR bands of both adsorbates and intermediates emerging between 1650 and 1200 cm⁻¹ show obvious increase with prolonged irradiation time. These observations can be ascribed to the fact that the O_{vs} could stabilize the carbonate radicals and increase their concentration on the catalyst surface by promoting charge separation and transfer to the adsorbed intermediates[19-20]. According to literature[21], the rate limiting step of CO_2 conversion to CO is the conversion of *COOH to *CO, which means the stabilized intermediates, including *COOH, cannot be readily converted to final products and explains the increase of enhanced signal of intermediate carbonates. In contrast, the peak at ~1700 cm⁻¹ corresponding to HCO_3^- remains unchanged under irradiation. This indicates that bicarbonate plays a different role from other adsorbates that have signals between 1650 and 1200 cm⁻¹. Recent reports[22-23] using *operando* ATR-SEIRAS discussed the effects of bicarbonate in liquid-solid interface reduction of CO_2, that is, the majority of CO_2 reactant near the catalyst surface originates from an equilibrium reaction with HCO_3^- rather than direct adsorption from the solution. Although there is still controversy in the process of CO_2 reduction[24], here based on our *in-situ* FT-IR results, it is reasonable to propose that in a gas phase reduction of CO_2 in the presence of H_2O vapor, CO_2 and surface adsorbed H_2O form HCO_3^- and release active species (denoted as ***init⁻*** in Eq. 1) participating in CO_2 reduction reaction[25]. The surface concentration of HCO_3^- in the equilibrium does not increase because CO_2 pressure can be seen as constant. This is consistent with the photocatalytic activity test in which $Ce_{0.6}Bi_{0.4}O_{2-\delta}$ shows much higher photocatalytic performance than CeO_2 (Fig. 1).

$$CO_2 \text{ (gas)} + H_2O_{ad} \leftrightarrow HCO_{3\ ad}^- + H^+ \leftrightarrow \textit{\textbf{init}}^- \quad \textbf{(Eq. 1)}$$

With the characteristic *in-situ* FT-IR bands and time related changes under irradiation, we proposed a pre-adsorption process that may shed new light into the mechanism of CO_2 photoreduction (Fig. 5)[26]. It is also evidenced that the introduction of Bi has created more O_{vs} and formed localized electrons, which show significant
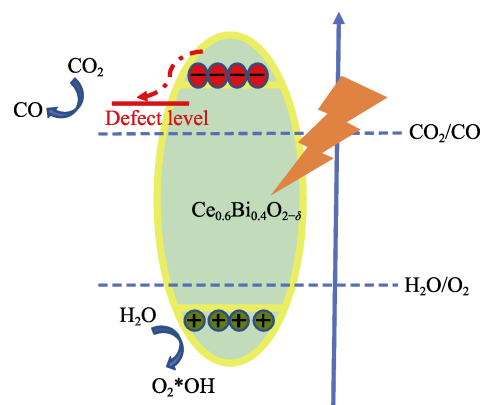

Fig. 5 Scheme of the possible mechanism of CO_2 reduction on $Ce_{0.6}Bi_{0.4}O_{2-\delta}$

benefit on the adsorption/activation behavior of CO_2 on the surface of the solid solution catalyst and promote the CO_2 photocatalytic activity of the catalyst.

3 Conclusions

In this work, Bi^{3+} with a lower valence and similar ion radius compared to Ce^{4+} has been doped into ceria forming a solid solution photocatalyst, from which it is concluded that:

1) Bi^{3+} doping successfully introduced O_{vs} into ceria while maintained its fluorite structure, thus the simultaneous introduction of defects as recombination sites of charge carriers could be effectively avoided;

2) The solid solution catalyst showed obviously improved CO_2 photocatalytic reduction activity with a CO yield ~4.6 times of that on pure ceria;

3) The favorable effects of O_{vs} and surface localized electrons on the adsorption/activation behavior of CO_2 on the catalyst surface and the separation/transfer of photoexcited carriers have been disclosed;

4) Doping aliovalent heteroatoms into metal oxide semiconductors to form solid solution catalysts is an effective way to introduce O_{vs} and promote photocatalytic activity.

Supporting materials

Supporting materials related to this article can be found at https://doi.org/10.15541/jim20200142.

References:

[1] CHANG X, WANG T, GONG J. CO₂ photo-reduction: insights into CO₂ activation and reaction on surfaces of photocatalysts. *Energy & Environmental Science*, 2016, **9(7):** 2177–2196.

[2] INDRAKANTI V P, KUBICKI J D, SCHOBERT H H. Photoinduced activation of CO₂ on Ti-based heterogeneous catalysts: current state, chemical physics-based insights and outlook. *Energy & Environmental Science*, 2009, **2(7):** 745–750.

[3] QI Y, SONG L, OUYANG S, *et al*. Photoinduced defect engineering: enhanced photothermal catalytic performance of 2D black In_2O_{3-x} nanosheets with bifunctional oxygen vacancies. *Advanced Materials*, 2019, **32**: 1903915.

[4] LINIC S, CHRISTOPHER P, INGRAM D B. Plasmonic-metal nanostructures for efficient conversion of solar to chemical energy. *Nature Materials*, 2011, **10(12)**: 911–921.

[5] LI J, SONG C F, PANG X J. Controllable synthesis and photocatalytic performance of $BiVO_4$ under visible-light irradiation. *Journal of Inorganic Materials*, 2019, **34(2)**: 164–172.

[6] SUN Y, WANG H, XING Q, *et al*. The pivotal effects of oxygen vacancy on Bi_2MoO_6: promoted visible light photocatalytic activity and reaction mechanism. *Chinese Journal of Catalysis*, 2019, **40(5)**: 647–655.

[7] WANG M, SHEN M, JIN X, *et al*. Oxygen vacancy generation and stabilization in CeO_{2-x} by Cu introduction with improved CO_2 photocatalytic reduction activity. *ACS Catalysis*, 2019, **9(5)**: 4573–4581.

[8] LIU Y, YU S, ZHENG K W, *et al*. NO Photo-oxidation and *in-situ* DRIFTS studies on N-doped $Bi_2O_2CO_3$/CdSe quantum dot composite. *Journal of Inorganic Materials*, 2019, **34(4)**: 425–432.

[9] JIANG D, WANG W, GAO E, *et al*. Bismuth-induced integration of solar energy conversion with synergistic low-temperature catalysis in $Ce_{1-x}Bi_xO_{2-\delta}$ nanorods. *Journal of Physical Chemistry C*, 2013, **117(46)**: 24242–24249.

[10] SHAMAILA S, SAJJAD A K L, CHEN F, *et al*. Study on highly visible light active Bi_2O_3 loaded ordered mesoporous titania. *Applied Catalysis B Environmental*, 2010, **94(3/4)**: 272–280.

[11] YANG G H, MIAO W K, YUAN Z M, *et al*. Bi quantum dots obtained *via in situ* photodeposition method as a new photocatalytic CO_2 reduction cocatalyst instead of noble metals: borrowing redox conversion between Bi_2O_3 and Bi. *Applied Catalysis B Environmental*, 2018, **237**: 302–308.

[12] GAO Y, LI R, CHEN S, *et al*. Morphology-dependent interplay of reduction behaviors, oxygen vacancies and hydroxyl reactivity of CeO_2 nanocrystals. *Physical Chemistry Chemical Physics*, 2015, **17(47)**: 31862–31871.

[13] CHEN D, HE D, LU J, *et al*. Investigation of the role of surface lattice oxygen and bulk lattice oxygen migration of cerium-based oxygen carriers: XPS and designed H_2-TPR characterization. *Applied Catalysis B Environmental*, 2017, **218**: 249–259.

[14] WEBER W H, HASS K C, MCBRIDE J R. Raman study of CeO_2: second-order scattering, lattice dynamics, and particle-size effects. *Physical Review B: Condensed Matter*, 1993, **48(1)**: 178–185.

[15] LI Y F, SOHEILNIA N, GREINER M, *et al*. $Pd@H_yWO_{3-x}$ nanowires efficiently catalyze the CO_2 heterogeneous reduction reaction with a pronounced light effect. *ACS Applied Materials & Interfaces*, 2019, **11(6)**: 5610–5615.

[16] ZHU S, LI T, CAI W B, *et al*. CO_2 Electrochemical reduction as probed through infrared spectroscopy. *ACS Energy Letters*, 2019, **4(3)**: 682–689.

[17] GAMARRA D, FERNANDEZ-GARCIA M, BELVER C, *et al*. Operando DRIFTS and XANES study of deactivating effect of CO_2 on a $Ce_{0.8}Cu_{0.2}O_2$. *Journal of Physical Chemistry C*, 2010, **114(43)**: 18576–18582.

[18] WANG Y, ZHAO J, WANG T, *et al*. CO_2 photoreduction with H_2O vapor on highly dispersed CeO_2/TiO_2 catalysts: surface species and their reactivity. *Journal of Catalysis*, 2016, **337**: 293–302.

[19] LI J, ZHANG W, RAN M, *et al*. Synergistic integration of Bi metal and phosphate defects on hexagonal and monoclinic $BiPO_4$: enhanced photocatalysis and reaction mechanism. *Applied Catalysis B Environmental*, 2019, **243**: 313–321.

[20] LI X, ZHANG W, LI J, *et al*. Transformation pathway and toxic intermediates inhibition of photocatalytic NO removal on designed Bi metal@ defective $Bi_2O_2SiO_3$. *Applied Catalysis B: Environmental*, 2019, **241**: 187–195.

[21] RINGE S, MORALES-GUIO C G, CHEN L D, *et al*. Double layer charging driven carbon dioxide adsorption limits the rate of electrochemical carbon dioxide reduction on gold. *Nature Communications*, 2020, **11(1)**: 33.

[22] DUNWELL M, LU Q, HEYES J M, *et al*. The central role of bicarbonate in the electrochemical reduction of carbon dioxide on gold. *Journal of the American Chemical Society*, 2017, **139(10)**: 3774–3783.

[23] ZHU S, JIANG B, CAI W B, *et al*. Direct observation on reaction intermediates and the role of bicarbonate anions in CO_2 Electrochemical reduction reaction on Cu surfaces. *Journal of the American Chemical Society*, 2017, **139(44)**: 15664–15667.

[24] WUTTIG A, YOON Y, RYU J, *et al*. Bicarbonate is not a general acid in Au-catalyzed CO_2 electroreduction. *Journal of the American Chemical Society*, 2017, **139(47)**: 17109–17113.

[25] YE L, DENG Y, WANG L, *et al*. Bismuth-based photocatalysts for solar photocatalytic carbon dioxide conversion. *ChemSusChem*, 2019, **12(16)**: 3671–3701.

[26] GRACIANI J, MUDIYANSELAGE K, XU F, *et al*. Highly active copper-ceria and copper-ceria-titania catalysts for methanol synthesis from CO_2. *Science*, 2014, **345(6196)**: 546–550.

铋掺杂提高氧化铈中氧空位浓度增强 CO_2 光催化还原性能

刘亚鑫[1,2]，王　敏[1,2]，沈　梦[1,2]，王　强[1,2]，张玲霞[1,2]

(1. 中国科学院 上海硅酸盐研究所, 高性能陶瓷和超微结构国家重点实验室, 上海　200050; 2. 中国科学院大学 材料科学与光电技术学院, 北京　100049)

摘　要: 氧空位在 CO_2 光催化还原过程中往往发挥重要作用。本工作中, 用水热法合成了不同 Bi 掺杂量的二氧化铈光催化剂 $Ce_{1-x}Bi_xO_{2-\delta}$, 其中 $Ce_{0.6}Bi_{0.4}O_{2-\delta}$ 在 Xe 灯照射下表现出最高的光催化活性, 其 CO 产率为纯二氧化铈纳米棒的 4.6 倍。X 射线衍射(XRD)分析表明固溶体保留了二氧化铈的萤石结构; 紫外–可见漫反射(UV-Vis)光谱表明固溶体可见光吸收增强; X 射线光电子能谱 (XPS)和拉曼光谱(Raman)分析表明, 掺杂后氧空位浓度明显提高。结合原位傅里叶变换红外光谱(*in-situ* FT-IR), 发现引入 Bi 提高了固溶体中氧空位的浓度, 并改变了 CO_2 在催化剂表面上的吸附/活化行为, 光照下碳酸氢根、碳酸根、甲酸等中间产物明显增多, 从而增强了 CO_2 光催化还原性能。

关　键　词: 光催化; CeO_2; CO_2 还原; Bi; 氧空位

中图分类号: O643　　　**文献标识码:** A

Supporting materials:

Bi-doped Ceria with Increased Oxygen Vacancy for Enhanced CO$_2$ Photoreduction Performance

LIU Yaxin[1,2], WANG Min[1,2], SHEN Meng[1,2], WANG Qiang[1,2], ZHANG Lingxia[1,2]

(1. State Key Laboratory of High Performance Ceramics and Superfine Microstructure, Shanghai Institute of Ceramics, Chinese Academy of Sciences, Shanghai 200050, China; 2. Center of Materials Science and Optoelectronics Engineering, University of Chinese Academy of Sciences, Beijing 100049, China)
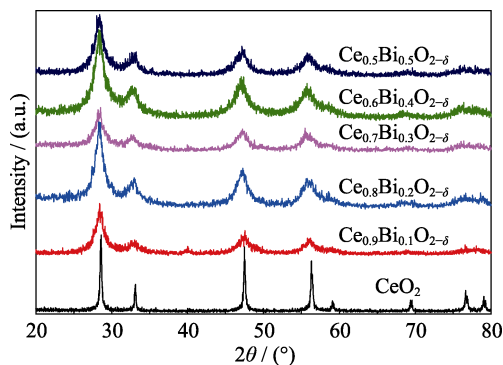

Fig. S1   XRD patterns of CeO$_2$ and Ce$_{1-x}$Bi$_x$O$_{2-\delta}$
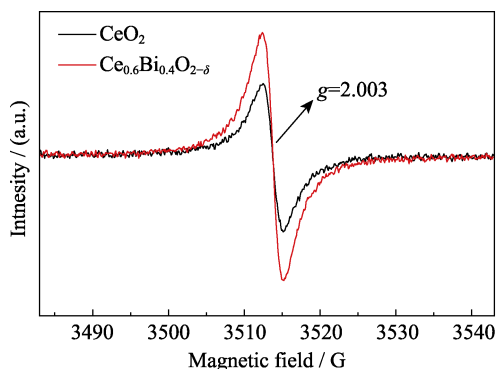
Fig. S2   EPR spectra of CeO$_2$ and Ce$_{1-x}$Bi$_x$O$_{2-\delta}$
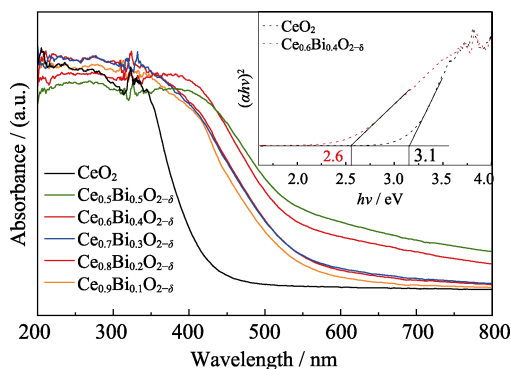
Fig. S3   UV-Vis absorption spectra of CeO$_2$ and Ce$_{1-x}$Bi$_x$O$_{2-\delta}$ with inset showing the plots of $(\alpha h\upsilon)^2$ *versus* photon energy
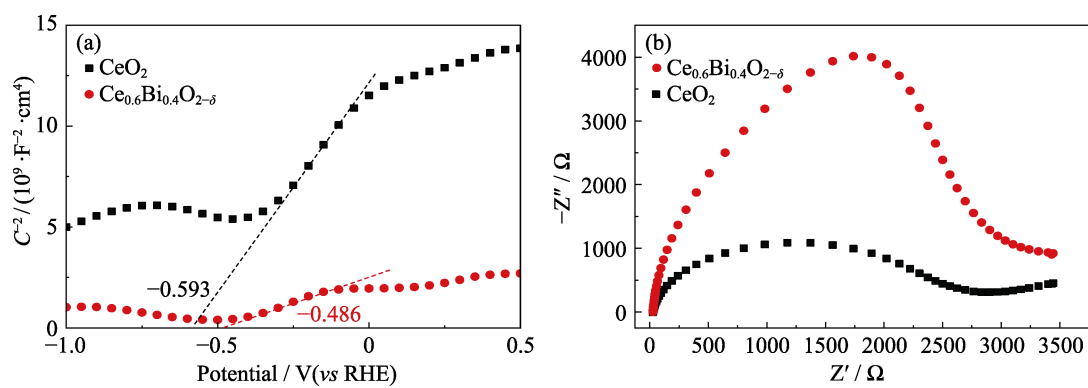
Fig. S4 (a) Mott-Schottky plots and (b) Electrochemical impedance spectroscopy (EIS) Nyquist plots (−0.4 V (*vs* Ag/AgCl), in dark) of CeO_2 and $Ce_{0.6}Bi_{0.4}O_{2-\delta}$
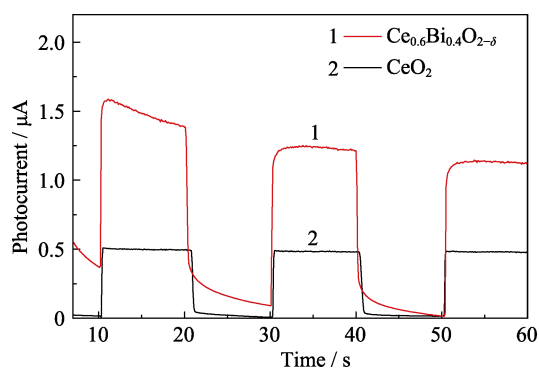

Fig. S5 Transient photocurrent responses of CeO_2 and $Ce_{0.6}Bi_{0.4}O_{2-\delta}$